Research Article

A catalyst-free new polyol method synthesized hot-pressed Cu-doped Bi_2S_3 nanorods and their thermoelectric properties

Tarachand[1], Vikash Sharma[1], Ranu Bhatt[2], Vedachalaiyer Ganesan[1], and Gunadhor Singh Okram[1] (✉)

[1] *UGC-DAE Consortium for Scientific Research, Indore 452001, India*
[2] *Technical Physics Division, Bhabha Atomic Research Centre, Mumbai 400085, India*

ABSTRACT

This is the first report on the thermoelectric properties of a catalyst-free polyol method used to prepare stoichiometric $Bi_{2-x}Cu_xS_3$ samples, x = 0.1, 0.2, 0.3, 0.4, via hot pressing. Various systematic approaches to arrive at in their stoichiometric compositions are explored precisely with introduction of excess precursor of S. X-ray diffraction data analysis using Rietveld refinement confirms a polyhedral orthorhombic crystal structure with a space group *Pnma*, in contrast to *Pbnm* reported earlier. Raman data further substantiates this. X-ray photoelectron spectroscopy confirms the valence states of the constituent elements (Bi^{3+}, Cu^{2+}, and S^{2-}) and energy dispersive X-ray analysis corroborates their compositions. The particle sizes of the pure Bi_2S_3 nanoparticles were 20, 35, and 82 nm as determined from the Scherrer formula, atomic force microscopy, and dynamic light scattering, respectively. Their transmission electron microscopy image shows rod-like nanostructures elongated in the <010> direction with an average diameter of 23 nm and a length of several hundreds of nanometers. A 34% improvement in the thermoelectric figure of merit is observed for $Bi_{1.6}Cu_{0.4}S_3$ as compared to pure Bi_2S_3 at 300 K.

1 Introduction

Bismuth sulfide (Bi_2S_3), a direct band gap (1.3–1.7 eV) semiconductor having a large absorption coefficient [1, 2], is an excellent candidate for fabrication of thermoelectric devices [3], visible-light photocatalytics [4], lithium ion batteries [5], solar cells, Schottky diodes [6], and gas sensors [7]. It belongs to the family of compounds of the type A_2X_3 (where A = Bi, Sb, Pb and X = S, Se, Te), which are considered among the most promising candidates for thermoelectric applications [8, 9]. However, so far the high resistance of Bi_2S_3 has been an obstacle to its commercial use [10–14]. Mizoguchi et al. [10] showed that the resistivity of Bi_2S_3 drops considerably as a result of vacuum annealing for both whiskers and pellets. They suggested

that this could be due to sulfur vacancies at the grain boundaries and in the bulk of the samples. Vacancies not only generate conduction electrons but also scatter phonons, resulting in significant suppression of resistivity (ρ) and thermal conductivity (κ). Chen et al. [14] found that ρ can be reduced by 5–6 orders of magnitude while maintaining a relatively large thermopower ($>300\ \mu\text{V}\cdot\text{K}^{-1}$) and low thermal conductivity by introducing sulfur vacancies into the lattice. The reason for the reduction was enhanced phonon scattering on sulfur vacancies, possible large numbers of weak ionic and chemical bonds with van der Waals forces [15]. Similar to S deficiency, studies of Se deficiency in $TiSe_2$ have been reported [16]. Enhanced selenium deficiency with increasing hot-press sintering temperature led to reduced resistivity and an improved dimensionless thermoelectric figure of merit, ZT, where T is the absolute temperature. The doping of transition metals in inorganic semiconductors (such as Bi_2X_3, X = Te, Se, S) prepared using a solid-state route and mechanical alloying in order to reduce the resistivity has been thoroughly studied [3, 17–20]. Ge et al. [20] found in $Bi_{2-x}Cu_xS_3$ that tailoring of the Cu content could reduce both the electrical resistivity and the thermal conductivity, which led to the high peak ZT value of 0.34 at 573 K for $Bi_{1.995}Cu_{0.005}S_3$. Recently, Biswas et al. [3] reported ZT values of up to 0.6 at 760 K for crystalline ingots of preferentially oriented Bi_2S_3, which greatly exceeds the previous value of powder-processed Bi_2S_3 samples.

In materials engineering, not only simple elemental doping but also nanostructuring has been very popular by theoretically proving the enhanced value of ZT [21]. As a result, researchers are much attracted to nanostructures synthesized by the chemical route because it allows them to manipulate such nanostructures on an atomic or molecular level. Thus, several types of Bi_2S_3 nanostructures have been synthesized by various methods such as hydrothermal or solvothermal routes, sonochemical techniques, electrochemical processes, and chemical vapor deposition, resulting in nanostructures of different sizes and shapes such as nanorods [22], nanowires [23], and nanotubes [24] and network-like [25], sphere-like [26], and flower-like [27] structures. Among all these synthetic processes, the polyol method [28, 29] is

an environmentally friendly yet inexpensive, non-hazardous, simple, quick, and versatile route to synthesizing colloidal dichalcogen particles [29, 30]. In this method, a metal precursor is heated in high-boiling-point alcohol ($\geq 200\ ^\circ\text{C}$) that acts as a surfactant, a reducing agent, or both.

As for bismuth telluride (Bi_2Te_3)-based alloys, even though they possess a ZT value close to 1 at approximately room temperature and are the best commercially available thermoelectric (TE) materials, they are rare and toxic due to the tellurium, which must therefore be replaced by a suitable element. In this context, a good choice is Bi_2S_3 because it contains naturally abundant and environmentally friendly elements. However, its resistance is high as compared to Bi_2Te_3 and Bi_2Se_3, and therefore it has received less attention. In this regard, Wang et al. [22] reported the synthesis of Bi_2S_3 nanorods by a polyol-assisted solvothermal method at 120 $^\circ$C for 62 h but concluded that the sample could not be synthesized in the absence of an extra base catalyst. In contrast, we report here the synthesis of Bi_2S_3 nanorods in the absence of any base catalyst using a simple polyol method. We optimized the reaction temperature and quantity of sulfur precursor within a span of only 2 h. Not only did we prepare stoichiometric samples successfully by a polyol method with vacuum annealing and Cu doping of Bi_2S_3 nanomaterials but also an enhanced ZT value was found.

2 Experimental

2.1 Synthesis process of Bi_2S_3 nanorods

In a typical synthesis, 2 mmol of $Bi(NO_3)_3\cdot 5H_2O$ ($\geq 98\%$, MERCK) and 7.5 mmol of thiourea (99%, MERCK) as Bi and S sources, respectively, were dissolved in 50 mL of diethylene glycol (DEG, $\geq 98.5\%$, MERCK). The mixture was transferred to a three-neck round-bottomed flask and heated in N_2 atmosphere at a rate of 6 $^\circ$C$\cdot$min^{-1}. The thiourea was taken in excess to take care of the volatile nature of sulfur. The solution immediately turned from a pinkish-yellow color to black at 97–100 $^\circ$C, which indicated the initial formation of Bi_2S_3 nanoparticles (NPs). However, for a better crystalline product and a complete reaction, the

temperature was maintained at 175–180 °C for 2 h with continuous flow of nitrogen gas. Then, the solution was allowed to cool naturally. Centrifugation for 12 min at 12,000 rpm and decantation removed the precipitate from the suspension. The precipitate was then dispersed in ethanol and subjected to 2 min of probe ultrasonication for uniform dispersion. The dispersed precipitate was then centrifuged for another 4 min at the same rpm, followed by 5 min of sonication. These cleaning steps were repeated three times. Finally, the transparent layer of ethanol was discarded and the precipitate was vacuum-dried at 60 °C for 1 h. The powder thus obtained was used for various characterizations and further processing. Notably, we optimized the reaction conditions, which were a temperature of 180 °C and a quantity of thiourea that was 2.5 times that of the nominally required amount. The samples are denoted as BSX, where X is the sample number. For Cu doping in bismuth sulfide ($Bi_{2-x}Cu_xS_3$, x = 0.1, 0.2, 0.3, 0.4), appropriate amounts of $Bi(NO_3)_3 \cdot 5H_2O$ were replaced by $Cu(NO_3)_2 \cdot 3H_2O$ (99%, MERCK); the other parameters remained the same.

2.2 Hot-press sintering

The as-prepared $Bi_{2-x}Cu_xS_3$, x = 0.1, 0.2, 0.3, 0.4, nanoparticles were highly resistive, and therefore needed further heat treatment. They were hot-press sintered in a vacuum of 10^{-5} mbar at 480 °C with an applied load of 10 kg for 1 h after optimizing them by sintering pure sample pellets at various temperatures. Details are given in the Electronic Supplementary Material (ESM).

2.3 Experimental techniques

The formation of a crystalline phase was characterized by X-ray diffraction (XRD) data collected using a Bruker D8 Advance/Bruker D2 Phaser X-ray diffractometer with Cu Kα radiation (1.54 Å) in an angle range (2θ) from 10° to 70°. Elemental analysis was performed by energy dispersive X-ray analysis (EDAX) using a Model JEOL JSM 5600 scanning electron microscope equipped with EDAX. The nanostructure and particle-size distribution were examined using atomic force microscopy (AFM), and measurements were performed

in air using an AFM NanoScope E (Digital Instruments) operated in contact mode. A silicon nitride-coated cantilever was used to probe different positions of the cold-pressed pellet surface. The hydrodynamic size and surface charge of the nanoparticles were measured in deionized water (as the suspension medium) at pH 7 and 25 °C using a zeta/particle-size analyzer (NanoPlus-3). Transmission electron microscopy (TEM) and high-resolution TEM (HRTEM) measurements were performed with a TECHNAI-20-G^2 system operated at a 200 kV accelerating voltage. Samples were prepared by dispersing the products in ethanol by ultrasonication and placing a drop of the suspension on a copper grid coated with an amorphous carbon film. For analysis of the chemical states of the constituent elements, X-ray photoelectron spectroscopy (XPS) measurements were performed on a X-ray photoelectron spectroscope (SPECS, Germany) using Al Kα radiation with an anode voltage of 13 kV and an emission current of 22.35 mA; a full-scan spectrum was recorded with an energy of 40 eV and a high-resolution spectrum was recorded with an energy of 30 eV. Raman spectroscopy measurements were performed using a LabRAM HR Visible instrument equipped with an Ar ion laser with a wavelength of 488 nm at room temperature. Seebeck coefficient (S) and resistivity measurements of the hot-pressed samples in the temperature range of 5–300 K were performed in a specially designed commercially available Dewar using differential direct current and a home-made four-point probe setup [31], respectively.

3 Results and discussion

3.1 XRD and EDAX analysis

To optimize the reaction conditions, four samples were synthesized at varying reaction temperatures using nominal amounts of the initial precursors (Fig. 1(a)). The characteristic peaks of the BS2 sample synthesized at 180 °C matched exactly those of the standard Bi_2S_3 patterns (JCPDS 652431), not for others. At higher reaction temperatures, many extra peaks appeared in addition to the characteristic peaks. At lower reaction temperatures, many characteristic peaks were invisible, indicating an incomplete reaction

below 180 °C and poor crystallinity.

We synthesized two more samples, namely BS14 and BS22, at 180 °C with double and triple the quantities of the initial precursors used in BS2 in order to increase the final yield. For BS14, one extra peak was found at 30.56° (Fig. 1(b)), which became more intense in BS22, indicative of enhanced oxidation into impurity phases.

The results corroborated the EDAX data, which showed a deficiency of sulfur but an excess of oxygen as a result of the formation of complexes of Bi, S, and oxygen or metal sulfite, $Bi–SO_X$ (Figs. 2(a) and 2(b)). To circumvent this oxide complex formation, we tried to take excess sulfur. This worked well, which is

evident in BS26 (Fig. 2(c)) and $Bi_{1.9}Cu_{0.1}S_3$ (Fig. 2(d)). The probable formation of H_2S or SO_2 gas could be one of the reasons for these results.

Therefore, an excess amount of thiourea was required to achieve the expected stoichiometry with better crystallinity. For further optimization of the quantities of the precursors, three samples were synthesized at 180 °C by taking 4.5, 6, and 7.5 mmol of thiourea with a fixed 3 mmol of bismuth nitrate. The samples are denoted as BS23, BS25, and BS26, respectively. Clear peak intensity enhancement with increasing thiourea concentration was evident from the XRD patterns (Fig. 3(a)). This indicates that the increase of thiourea led to an improvement in the
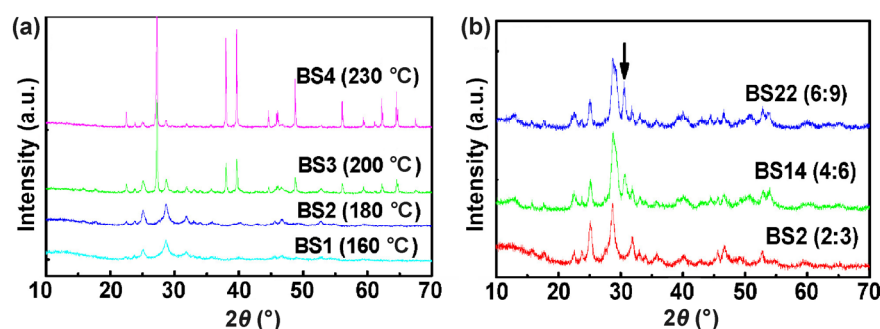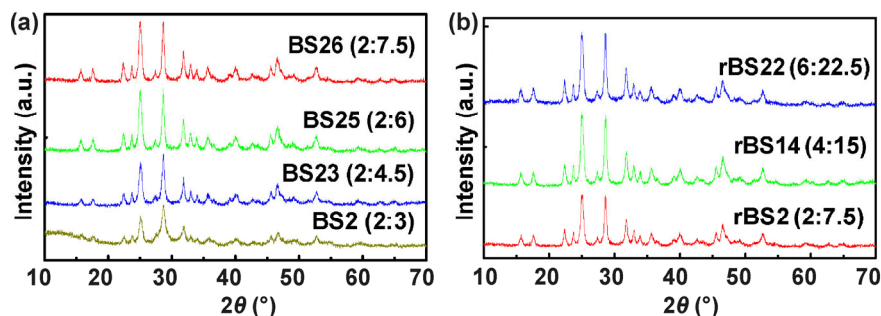

Figure 1 (a) XRD patterns of nominal Bi_2S_3 prepared at the reaction temperatures indicated; the optimum temperature is 180 °C. (b) Nominal quantity variation of both Bi and S precursors (in mmol) at 180 °C. Arrow indicates impurity peak.
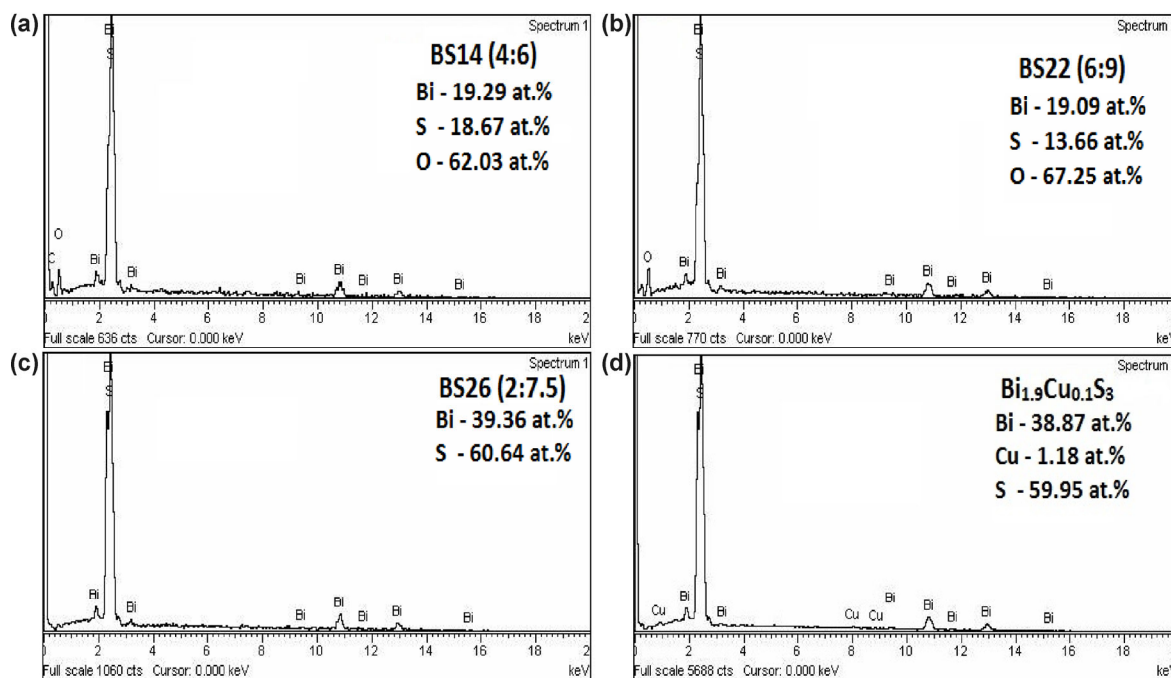
**Figure 2** EDAX spectra of (a) BS14, (b) BS25, (c) BS26, and (d) $Bi_{1.9}Cu_{0.1}S_3$ samples.

Figure 3 XRD patterns of quantity variation of (a) sulfur source with fixed Bi source and (b) both sources with optimized quantity of sulfur precursor.

crystalline quality and hence to suppressed background noise, along with relatively more intense peaks. This was checked for quantities up to 2.5 times the nominally required quantity. The EDAX pattern of BS26 (Fig. 2(c)) showed the ratio of Bi:S as 39.36:60.64 for the cold-pressed pellet of Bi_2S_3, indicating no sulfur deficiency in the final product, which is in good agreement with the theoretical stoichiometry of Bi_2S_3 without oxygen. The particle size calculated from the Scherrer formula for BS26, which had the best crystallinity, was 20 nm. The results for BS2, BS14, and BS22 (Fig. 1(b)) and for BS23, BS25, and BS26 (Fig. 3(a)) motivated us to look for further improvement in the quality and yield of the samples prepared. We therefore re-synthesized the BS2, BS14, and BS22 samples at 180 °C with the optimized quantity of thiourea, denoting the samples as rBS2, rBS14, and rBS22, respectively (Fig. 3(b)). In these samples, no extra peak at 30.56° was found and all peaks were well-matched with single-phase Bi_2S_3 (JCPDS 652431).

After optimizing the reaction conditions, we synthesized a series of Cu-doped bismuth sulfide,

$Bi_{2-x}Cu_xS_3$, x = 0.1, 0.2, 0.3, 0.4, nanoparticles and found that all samples exhibited a single phase (Fig. 4(a)). However, the peak intensities decreased somewhat as the Cu doping increased, which is indicative of modified unit cells with doping. Figure 2(d) shows the typical EDAX pattern of the cold-pressed pellet of the $Bi_{1.9}Cu_{0.1}S_3$ sample. The figure shows the atomic percentage ratio of Bi:Cu:S as 38.87:1.18:59.95, indicating a slightly lower copper content. This implies some interesting behavior of the Cu-doped samples. Therefore, further EDAX data were collected for the $Bi_{2-x}Cu_xS_3$, x = 0.2, 0.3, 0.4, samples. The collected data are shown in Fig. S2 (in the ESM) and presented in Table 1. It is clear that although Bi and S maintained their theoretical contents (at.%), Cu showed contents of 2.87 at.%, 4.82 at.%, and 6.71 at.% instead of the theoretical 4 at.%, 6 at.%, and 8 at.%, indicating a Cu deficiency, irrespective of the sample. This may be most probably due to Cu removal during centrifugation as CuS because CuS is lighter than $Bi_{2-x}Cu_xS_3$, which agrees with the XPS data (Fig. 5) that suggests presence of Cu^{2+}, S^{2-}, and Bi^{3+} states, not in elemental states,
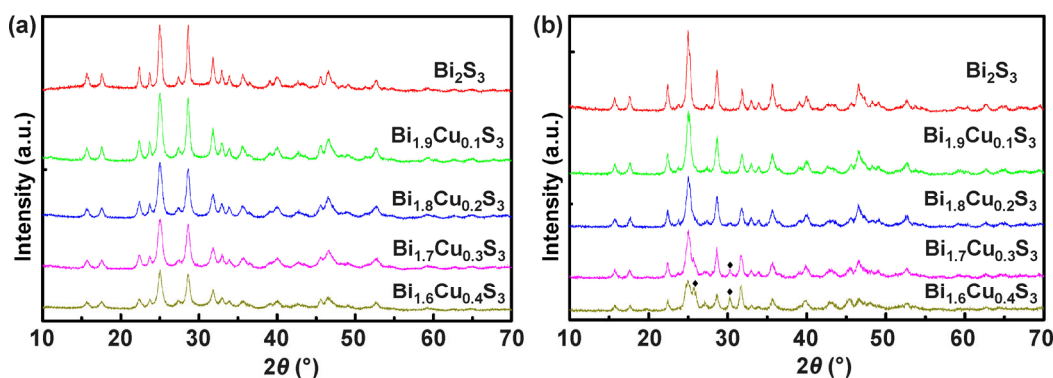
Figure 4 XRD patterns of $Bi_{2-x}Cu_xS_3$, x = 0.1, 0.2, 0.3, 0.4, (a) before and (b) after hot-press pelletization.
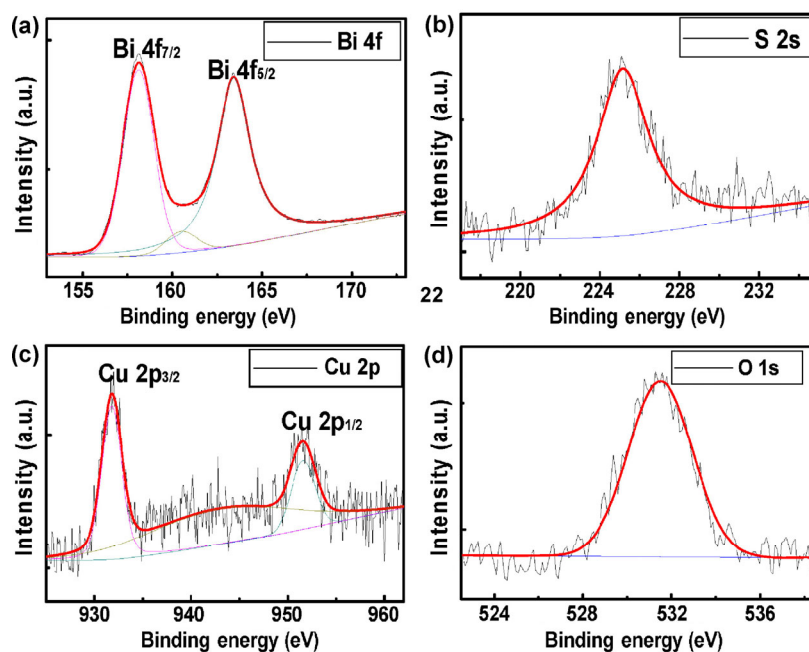
Figure 5 High-resolution XPS spectra of (a) Bi 4f, (b) S 2s, (c) Cu 2p, and (d) O 1s of the $Bi_{1.9}Cu_{0.1}S_3$ sample. Experimental XPS data are noisy curves and continuous smooth curves are software-fitted peaks.

Table 1 The atomic percentage ratios of Bi:Cu:S in $Bi_{2-x}Cu_xS_3$, $x = 0$–0.4, samples

Nominal chemical formula	Bi (at.%)	Cu (at.%)	S (at.%)
Bi_2S_3	39.36	0.0	60.64
$Bi_{1.9}Cu_{0.1}S_3$	38.87	1.18	59.95
$Bi_{1.8}Cu_{0.2}S_3$	36.36	2.87	60.77
$Bi_{1.7}Cu_{0.3}S_3$	35.17	4.82	60.02
$Bi_{1.6}Cu_{0.4}S_3$	33.85	6.71	59.45

and also its valence states would be immaterial in either CuS or $Bi_{2-x}Cu_xS_3$. Further details on CuS formation is discussed later.

These as-prepared samples required further hot-pressing treatment to reduce their resistivity and enhance other transport properties. The diffraction peaks of hot-pressed pellets of BS26 were somewhat narrower (Fig. 4(b)) than those of the as-prepared Bi_2S_3 sample (Fig. 4(a)). This is attributed to the enhanced crystallite size, from 20 to 22 nm, after hot pressing. However, in the hot-pressed samples, second-phase peaks due to $Bi_{4.8}Cu_{2.94}S_9$ (JCPDS 655469), as indicated by the filled diamond (♦) sign for $x = 0.3$ and 0.4, are seen clearly, whereas only vestiges of second-phase peaks for $x = 0.1$ and 0.2 are apparent. A composition similar to that of $Bi_{4.8}Cu_{2.94}S_9$ that matched the impurity

phase formed after the hot-press procedure at 472 °C was reported [32, 33]. The generation mechanism of this composition may therefore be described as follows. When Bi_2S_3 is doped with Cu, a mixture of an impurity CuS phase with the majority Bi_2S_3 or $Bi_{2-x}Cu_xS_3$ phase may be formed owing to the low reaction temperature (180 °C), whereas Cu might not replace Bi easily because of the large difference in their ionic radii [34]. The concentration of the CuS phase may be too low as compared to the major host Bi_2S_3 or $Bi_{2-x}Cu_xS_3$ phase, giving rise therefore to no observable extra peaks in the powder XRD patterns (Fig. 4(a)). However, when Cu-doped Bi_2S_3 samples are hot pressed at 480 °C, a transformation appears to take place to form $Bi_{4.8}Cu_{2.94}S_9$, as observed, as in the following reaction

$$4.8Bi_2S_3 + 2.94CuS \xrightarrow[1\,h]{480\,°C} 2.4\ Bi_2S_3 +$$
$$Bi_{4.8}Cu_{2.94}S_9 + 1.14\ S^{2-}\uparrow \qquad (1)$$
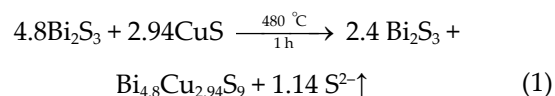
To ascertain the crystal structure precisely, we performed structural Rietveld refinement by using FullProf software for the XRD patterns of the as-prepared $Bi_{2-x}Cu_xS_3$, where $x = 0$–0.4, and hot-pressed (HP) pure Bi_2S_3. The initial refinement parameters were taken from Lundegard et al. [35]. The refined

XRD graphs for the as-prepared pure Bi_2S_3 in powder form, as well as the HP pellets, are shown in Fig. 6; those of the other samples are shown in Fig. S1 (in the ESM). Note that Rietveld fitting using the space group *Pbnm* could not be fit; however, space group *Pnma* could be fit. Because of this, to our knowledge, there is no report on the Rietveld fitting of this compound. This was related to the exchange of lattice parameters *a*, *b*, and *c*.

The data in Table 2 are rather intriguing. Although parameter *a* varies somewhat randomly, parameters *b* and *c* somewhat decrease and increase, respectively, with increasing Cu content. This is evidence of the replacement of smaller atomic radii Cu atoms for larger atomic radii Bi atoms in the lattice of Bi_2S_3. These data therefore prove that copper was successfully doped in Bi_2S_3. Accordingly, the unit cell volume decreased somewhat marginally with increasing Cu content, although not very systematically, with the exception of $Bi_{1.6}Cu_{0.4}S_3$. This suggests that doping of Cu in the Bi_2S_3 lattice was not very straightforward, showing complicacy in its lattice structure, which might be beneficial in terms of the thermoelectric

properties.

In this scenario, looking into the crystal structure of Bi_2S_3 (Fig. 7(a)) may be interesting. The crystal structure of bismuth sulfide with space group *Pnma* consists of tightly bonded infinite $(Bi_4S_6)_n$ ribbons extending along the <010> direction in a herringbone arrangement (Figs. 7(b) and 7(d)). There are two independent Bi positions, Bi1 at the margin of the Bi_4S_6 ribbon and Bi2 placed around the center of the ribbon. Kyono et al. [36] reported that the Bi1 sites can be coordinated to seven ligand atoms of sulfur with three short and strong bonds and four weak and long bonds, whereas the Bi_2 sites are also seven-coordinated but with five short and strong bonds and two weak and long bonds. These five short bonds are arranged at the vertices of a square pyramid (Fig. 7(c)), and below these square pyramids lone-pair electrons of Bi2 are interposed between the two longer bonds. Although both positions are seven-coordinated (Fig. 7(c)) in relation to the 4 Å axis, Bi1-S_7 is a monocapped "lying" prism, whereas Bi2-S_7 is a "standing" prism [35]. The Bi1 polyhedrons are perpendicular to the *b* axis, and therefore they are monocapped lying
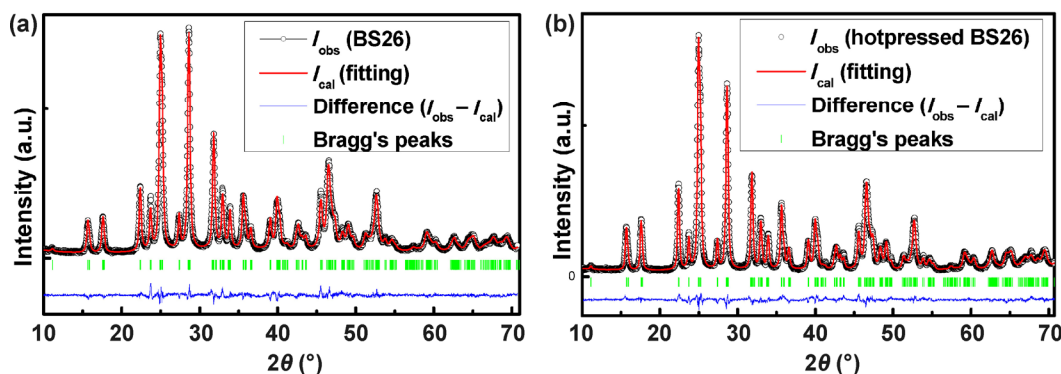
Figure 6 Structural Rietveld refinement of XRD patterns of BS26 as (a) a powder and (b) a hot-pressed pellet with slow scan rate.

Table 2 Lattice parameters and density of the compound obtained after Rietveld refinement for powder XRD patterns of $Bi_{2-x}Cu_xS_3$, $x = 0–0.4$, and HP-pellet XRD pattern of Bi_2S_3

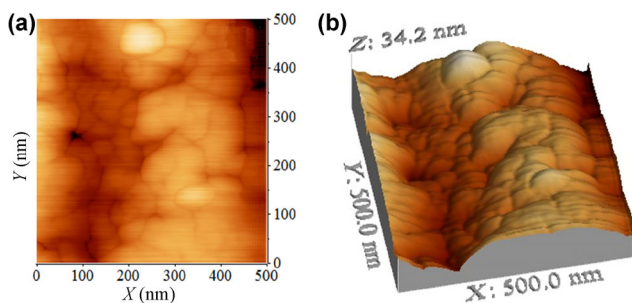| Parameter	BS26 powder	$x = 0.1$ powder	$x = 0.2$ powder	$x = 0.3$ powder	$x = 0.4$ powder	HP Bi_2S_3 pellet
a (Å)	11.315	11.316	11.318	11.312	11.327	11.299
b (Å)	3.986	3.981	3.983	3.982	3.980	3.982
c (Å)	11.161	11.157	11.158	11.152	11.163	11.148
V (Å^3)	503.334	502.53	502.898	502.318	503.267	501.609
ρ_v (g/cm^3)	6.785	6.683	6.510	6.339	6.151	6.808
χ^2 value	2.14	1.22	1.23	1.170	1.05	2.18
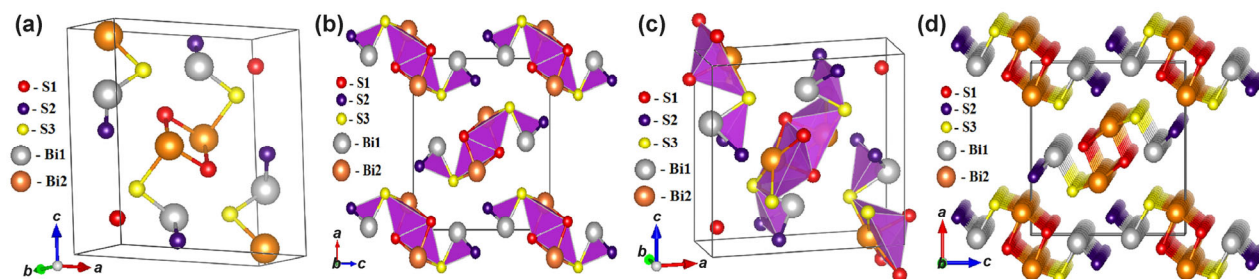
Figure 7 Three-dimensional (3D) crystal structure of Bi_2S_3. (a) A unit cell, which contains 4 molecules (20 atoms), (b) two-dimensional (2D) polyhedral structure of $(Bi_4S_6)_n$, (c) polyhedral crystal structure of unit cell by taking additional atoms if any atoms are included in the boundary, and (d) slightly tilted structure of $(Bi_4S_6)_n$ ribbons, which show infinite chains attached to Bi_4S_6 rods parallel to the b axis.

prisms, whereas $Bi2S_7$ polyhedrons are standing prisms because they are parallel to the b axis.

3.2 Microstructure studies

3.2.1 Atomic force microscopic study

In order to understand the morphology of the samples, typical 2D and 3D AFM images of the BS26 sample are shown in Figs. 8(a) and 8(b), respectively. The scan size is 500 nm and the scan rate is 15.26 Hz. In the 2D image, a large number of small clusters roughly 100 nm in size are present, and these clusters themselves consist of many sub-particles with an average diameter of 35 nm. These particles are either spherical or elliptical in shape with slight variations in size, which indicates the polycrystalline nature of Bi_2S_3 nanoparticles. Larger clusters are due to aggregation of the smaller particles because the pellets were compacted using ~1 GPa pressure. Here, the average size of the small particles is 35 ± 5 nm, with particle sizes ranging from approximately 20 to 100 nm. This average particle size is greater than the crystallite

size calculated from XRD (20 nm) that was theoretically expected.

3.2.2 Transmission electron microscopic study

To obtain a more accurate nanoparticle size, TEM measurements were carried out for BS26. Figure 9 shows a typical TEM image of the as-synthesized Bi_2S_3 sample. This image reveals that the product consists of many quite uniform nanorods and that their diameters are in the range of 12–49 nm, with an average diameter of ~23 nm, and that they have a length of several hundreds of nanometers (Figs. 9(a) and 9(b)). An HRTEM image of Bi_2S_3 nanorods is shown in Fig. 9(c), which shows the clear single-crystal structure of a nanorod with a regular estimated fringe spacing of 0.798 nm, which is in good agreement with d value of the [101] crystal planes of orthorhombic-phase Bi_2S_3 parallel to the axis of the nanorods. This implies that the nanorod axis elongates in the <010> direction [15]. Figure 9(d) shows the selected area electron diffraction (SAED) pattern of a nanorod, which clearly shows that the constituent Bi_2S_3 nanorod is a single crystal. On the other hand, dynamic light-scattering (DLS) data (see ESM for details) showed the particle size as 82 nm.

3.3 X-ray photoelectron spectroscopic studies

The valence states of the constituent elements in the resulting product were studied by X-ray photoelectron spectroscopy. To calibrate the spectra, the binding energy (BE) of carbon (C 1s) was used as the internal reference. Full-scan data were recorded from 0 to 1,000 eV, as shown in Fig. S4 (in the ESM). The high-


Figure 8 (a) 2D AFM image and (b) 3D image of Bi_2S_3 nanoparticles (BS26).
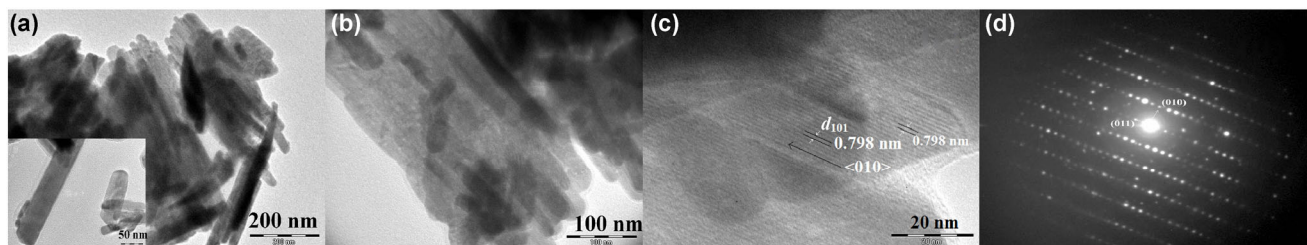
Figure 9 (a), (b), and inset of (a) Transmission electron microscopy images of Bi_2S_3 nanorods (BS26) at different magnifications. (c) HRTEM image and (d) SAED pattern of nanorods.

resolution spectra of Bi 4f, Cu 2p, and S 2s were recorded to determine the oxidation states of the constituent elements. They were fitted with XPS peak software, as shown in Figs. 5(a)–5(d). BEs of Bi $4f_{7/2}$ and $4f_{5/2}$, found at 158.1 and 163.4 eV, respectively, at two peaks have a constant separation of 5.3 eV over the entire region of the compounds, corresponding to the Bi^{3+} chemical state (Fig. 5(a)) [37]. This confirms the presence of the Bi^{3+} state in Bi_2S_3. The peak of Bi $4f_{5/2}$ was somewhat asymmetric because of merging with the S 2p peak at 160.5 eV, which is clearly seen in the de-convoluted graph. The binding energy of the S 2s peak (Fig. 5(b)) found at 225.1 eV is consistent with the S^{2-} state in Bi_2S_3 [15]. Figure 5(c) shows the high-resolution spectrum of Cu 2p, with BEs of the Cu $2p_{3/2}$ and $2p_{1/2}$ peaks at 931.79 and 951.58 eV, respectively, with a separation of 19.79 eV. The peak at 931.79 eV is characteristic of Cu^{2+}, and it is 1.1 eV lower than that of the typical Cu^+ [38, 39]. In addition, the very weak broad peak at 943 eV corresponds to

the satellite peak ($KL_{23}L_{23}$) of Cu^{2+} [40]. The oxygen peak at 531.5 eV (Fig. 5(d)) is due to either O_2 molecules or surfactant associated/adsorbed on the surfaces of the NPs because normal oxide peaks have higher energies.

3.4 Raman spectroscopic studies

Raman spectroscopy is an effective tool for structural characterization. The Raman spectra of samples synthesized with different quantities of the sulfur precursor while the bismuth source remained fixed were recorded in the frequency range 50–600 cm^{-1} at 300 K (Fig. 10(a)). Figure 10(b) shows the multi-peak Lorentzian fitting of the experimental Raman spectrum of BS26, which was synthesized with a Bi:S initial precursor ratio of 2:7.5 mmol; the results for the other samples are shown in Fig. S5 (in the ESM). The Raman mode positions, along with their full width at half maximum (FWHM), are listed in Table 3. The observed Raman modes for the BS26 sample at 87.58, 99.82, 125.38, 168.18, 186.62, 236.43, 261.45, and 275.07 cm^{-1}
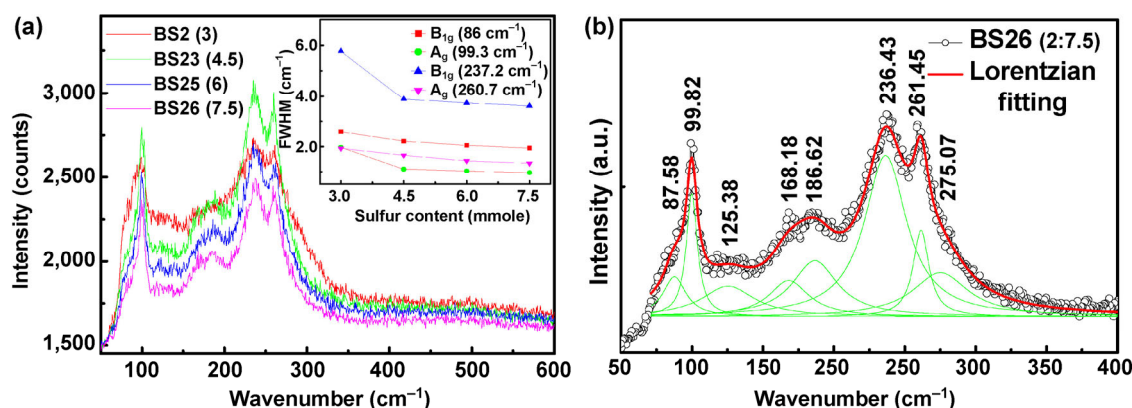
Figure 10 (a) Raman spectra of samples synthesized with different quantities of S precursor (thiourea, written in brackets) with fixed 2 mmol Bi source. Inset: effect of S content on FWHM of B_{1g} modes at 86 and 260.7 cm^{-1} and A_g mode at 99.3 and 237.2 cm^{-1}. (b) Multi-peak Lorentzian fitting (red solid line) from summation of all the Lorentzian (green) curves of the experimental Raman spectrum (open circle) of the BS26 (2:7.5) sample. Numbers indicated are the fitted peak positions in cm^{-1}.

Table 3 Raman phonon modes (ν_p) and FWHM ($\Delta\nu_p$) obtained through first-principles calculations [41] and the experimental values by Lorentzian peaks fitting in Bi_2S_3 for varying S for fixed Bi

Raman mode (theoretical ν_p in cm⁻¹, Ref. [41])	BS2 (2:3) ν_p ($\Delta\nu_p$) (cm⁻¹)	BS23 (2:4.5) ν_p ($\Delta\nu_p$) (cm⁻¹)	BS25 (2:6) ν_p ($\Delta\nu_p$) (cm⁻¹)	BS26 (2:7.5) ν_p ($\Delta\nu_p$) (cm⁻¹)
B_{1g} (86)	85.23 (25.93)	85.57 (22.2)	87.24 (20.56)	87.58 (19.49)
A_g (99.3)	98.16 (19.71)	99.93 (11.01)	99.81 (10.26)	99.82 (9.57)
B_{3u} (119.3)	125.41 (40.6)	125.83 (35.46)	125.63 (42.62)	125.38 (44.96)
B_{1g} (173.4)	176.78 (84.61)	167.92 (33.58)	168.03 (35.29)	168.18 (34.03)
A_g (184)	—	187.96 (44.06)	186.85 (40.31)	186.62 (38.80)
A_g (237.2)	235.91 (57.72)	235.88 (38.87)	236.24 (37.32)	236.43 (36.21)
B_{1g} (260.7)	262.10 19.37)	260.73 (16.6)	261.63 (14.32)	261.45 (13.42)
B_{1g} (277.3)	287.10 (46.13)	276.59 (35.52)	275.01 (49.27)	275.07 (47.52)

are much closer to the reported theoretical and experimental values [41, 42].

The observed Raman modes unambiguously identify the orthorhombic phase of Bi_2S_3, which is consistent with the XRD data (Fig. 3(a)). No impurity modes were detected in the case of thiourea amounts greater than 3 mmol in the synthesis, i.e., in BS23, BS25, and BS26. In particular, no extra peak from the Bi–O mode was observed, which generally shows Raman bands at approximately 117–118, 310–314, 430–432, and 519–525 cm⁻¹ [43, 44]. In the case of BS2 (2:3), one A_g mode at 184 cm⁻¹ merged with the B_{1g} mode at 173.3 cm⁻¹ and one B_{1g} mode at 277.3 cm⁻¹ is observed at 287.1 cm⁻¹, with a large deviation of ~10 cm⁻¹. Other modes were broadened and much deviated from the theoretically estimated value, which is attributed to the non-stoichiometric Bi_2S_3 of the BS2 sample.

Deviation from the original positions and broadening of the modes could also be related to its reduced size (Table S1 in the ESM). The intensity of all the Raman modes (Fig. 10(a)) and FWHMs of the B_{1g} modes at 86 and 260.7 cm⁻¹ and the A_g modes at 99.3 and 237.2 cm⁻¹ decreased with increasing S content (Fig. 10(a), inset). This trend is consistent with the decrease in average

particle size (Table S1 in the ESM) of the samples, and it is in agreement with an earlier report [45]. This can be explained based on the Raman intensity dependence on the quantum dot radius (R) as R^{-3} for the optical deformation potential mechanism [45, 46].

3.5 Resistivity and thermopower

The resistivity (ρ) of cold-pressed (1 GPa at 27 °C) pellets of pure Bi_2S_3 was very high (Fig. 11), and hence high-temperature sintering was needed to reduce it [3, 10–14]. For this, hot-press sintering was performed at 27, 200, 320, 480, and 520 °C in vacuum (10⁻⁵ Torr) under 10 kg axial force for 1 h to consolidate Bi_2S_3 NPs into pellets and to determine the optimum sintering temperature. A negligible reduction in ρ was observed for the first hot-pressed sample at 200 °C as compared to that made at 27 °C (Fig. 11). With increasing hot-press sintering temperature, ρ decreased systematically (Fig. 11, inset). This reduction in ρ is attributed to the formation of sulfur vacancies and the increase in density by removing porosity. Here, each sulfur vacancy provided two free electrons to the host lattice; this increase in the number of sulfur vacancies led to the characterization of Bi_2S_3 as an n-type semiconductor [3, 10–14]. Although the ρ value of the sample hot pressed at 520 °C was the lowest (Fig. 11, inset), but organic, moiety-related fume came
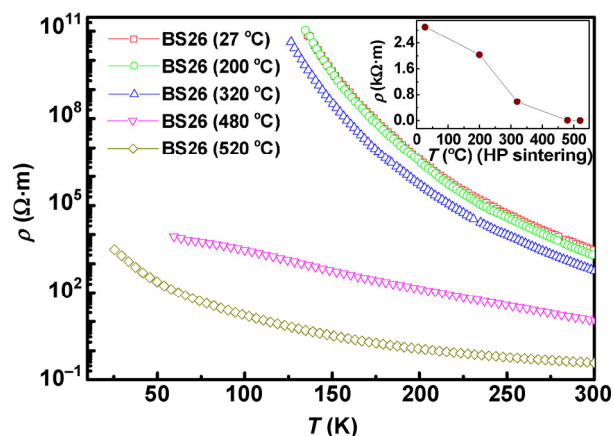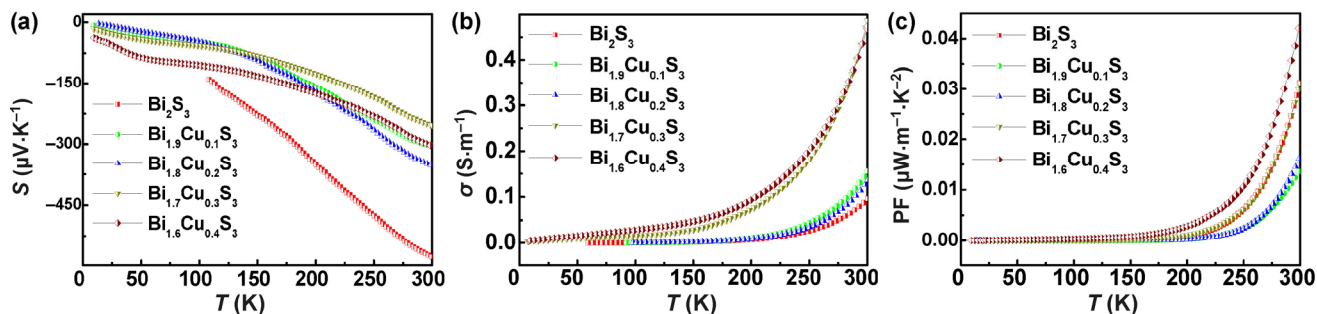

Figure 11 Temperature dependence of ρ of Bi_2S_3 (BS26) nanorods hot pressed at 27, 200, 320, 480, and 520 °C. The ρ values of the HP samples at 27, 200, and 320 °C were measured by using the two-probe method, whereas those at 480 and 520 °C were measured by the four-probe method. The errors in the measurements were 5% and 3%, respectively [31]. The inset shows the effect of hot-press sintering temperature on ρ at 300 K.

out during hot pressing. Therefore, all the doped samples, i.e., $Bi_{2-x}Cu_xS_3$, x = 0.1, 0.2, 0.3, 0.4, were hot-pressed at 480 °C and their Seebeck coefficients (S) and electrical conductivities (σ) were investigated in the temperature range of 5 to 300 K (Figs. 12(a) and 12(b)). It is pointed out here that because their crystal structure was peculiar and hot pressed, we checked the direction-dependence of the S and σ data for the hot-pressed pellets parallel and perpendicular to the applied force. A typical example of measurements on pure Bi_2S_3 is shown in Fig. S6 (in the ESM). Their absolute values along the parallel direction were in general relatively more than those along the perpendicular direction that gave higher power factor. These configurations were used in all the data presented. The S values ranged from −3 to −353 $\mu V \cdot K^{-1}$ for all doped samples, whereas for pure Bi_2S_3 the maximum absolute value was 577 $\mu V \cdot K^{-1}$ at 300 K. The negative sign of S indicates that the majority charge carriers were electrons for the whole temperature range of the investigation.

The electrical conductivity σ (Fig. 12(b)) increased with increasing Cu content, indicating the increasing electron concentration as S shows n-type conduction (Fig. 12(a)). Further, σ increased exponentially with temperature, thus showing semiconducting behavior. Around 300 K, all the $Bi_{2-x}Cu_xS_3$, x = 0.1–0.4, samples possessed higher σ values as compared to pure Bi_2S_3. This increase in σ was much more significant for x = 0.3 and 0.4. This is understood tentatively to be due to the formation of a probably more conducting second phase, $Bi_{4.8}Cu_{2.94}S_9$ (JCPDS 655469), as seen in the XRD results (Fig. 4(b)). This higher conductivity is based on a probable excess of Cu content, and hence on the

extra electrons of $Bi_{4.8}Cu_{2.94}S_9$ as compared to, say, $Bi_{1.6}Cu_{0.4}S_3$ because when $Bi_{1.6}Cu_{0.4}S_3$ is multiplied by 3, $Bi_{4.8}Cu_{1.2}S_9$ is obtained. This is inconsistent with the better conductivity (4.3 $S \cdot cm^{-1}$) in $CuBiS_2$ [32]. The above results showing the probable enhanced electron concentration with increasing Cu content are in good agreement with the Ioffe theory [47] up to x = 0.3. According to this theory, the Seebeck coefficient for most metals and semiconductors is inversely proportional to the carrier concentration.

Although the x = 0.3 and 0.4 samples show almost equal σ values at 300 K, the value of S for the x = 0.4 sample is higher than that for the x = 0.3 sample in the 5–300 K range, which cannot be explained by the Ioffe theory. This may be due to a competitive process in contributing carriers from $Bi_{1.6}Cu_{0.4}S_3$ and $Bi_{4.8}Cu_{2.94}S_9$ that favor an enhanced S value but almost the same σ value as that of the 0.3 sample. This could lead to an enhanced power factor (PF). This in fact is observed, and it is the highest of all samples at 300 K. In PF (Fig. 12(c)), a 34% enhancement was seen at 300 K for hot-pressed pellets of $Bi_{1.6}Cu_{0.4}S_3$ as compared to the pure sample, whereas all the other doped samples showed PF values lower than that of the pure sample. If we take the value of the thermal conductivity (κ) of bulk Bi_2S_3, which is 0.7 $W \cdot m^{-1} \cdot K^{-1}$ according to the literature [13], then the ZT value turns out to be enhanced from 1.34×10^{-5} to 1.8×10^{-5} at 300 K, which is a 34% enhancement for the $Bi_{1.6}Cu_{0.4}S_3$ sample (Table S2 in the ESM). The estimated low value of ZT is attributed to the absence of their actual thermal conductivity data and better stoichiometry. However, the present nanorods of the Bi_2S_3 and Cu-doped samples synthesized by the chemical route are likely

Figure 12 Temperature dependence of (a) Seebeck coefficient, (b) electrical conductivity, and (c) power factor for $Bi_{2-x}Cu_xS_3$, where x = 0.1–0.4 for hot pressing at 480 °C.

to have significantly reduced values of κ that may consequently result in much larger ZT values.

4   Conclusions

Nanostructured $Bi_{2-x}Cu_xS_3$ ($x = 0.1$–0.4) samples were successfully synthesized by a simple polyol method without using any base catalyst. The particle size determined from XRD, AFM, TEM, and DLS was in good accordance with the theoretical size. The individual nanorods showed a single crystalline structure, which played a very important role in the transport properties. The presence of obvious B_{1g} (87.58, 168.18, 261.45, and 275.07 cm^{-1}) and A_{1g} (99.82, 186.62, and 236.43 cm^{-1}) optical modes of the Bi–S bonds in the Raman data confirmed that the Bi_2S_3 nanostructure was perfectly synthesized. In addition, a reduction in electrical resistivity by hot-press sintering and Cu doping was demonstrated. The rod-like structure of Bi_2S_3 appeared to play a very important role in achieving a high Seebeck coefficient. The absolute value of the thermopower decreased with increasing Cu doping. Consequently, an enhancement in the figure of merit of 34% was observed for the $Bi_{1.6}Cu_{0.4}S_3$ sample as compared to undoped Bi_2S_3 at 300 K.

Acknowledgements

Electronic Supplementary Material: Supplementary material (brief details of hotpress sintering, used characterizations like XRD, TEM, Raman spectroscopy and dynamic light scatering measurements, figures of Rietveld refinement, EDAX, XPS, DLS and Raman data and tables of calculated crystallite sizes and ZT values) is available in the online version of this article at http://dx.doi.org/10.1007/s12274-016-1207-6.

References

[1] Riley, D. J.; Waggett, J. P.; Wijayantha, K. G. U. Colloidal bismuth sulfide nanoparticles: A photoelectrochemical study of the relationship between bandgap and particle size. *J. Mater. Chem.* **2004**, *14*, 704–708.

[2] Larson, P.; Greanya, V. A.; Tonjes, W. C.; Liu, R.; Mahanti, S. D.; Olson, C. G. Electronic structure of Bi_2X_3 (X = S, Se, T) compounds: Comparison of theoretical calculations with photoemission studies. *Phys. Rev. B* **2002**, *65*, 085108.

[3] Biswas, K.; Zhao, L. D.; Kanatzidis, M. G. Tellurium-free thermoelectric: The anisotropic n-type semiconductor Bi_2S_3. *Adv. Energy Mater.* **2012**, *2*, 634–638.

[4] Liu, Z. Q.; Huang, W. Y.; Zhang, Y. M.; Tong, Y. X. Facile hydrothermal synthesis of Bi_2S_3 spheres and CuS/Bi_2S_3 composites nanostructures with enhanced visible-light photocatalytic performances. *CrystEngComm* **2012**, *14*, 8261–8267.

[5] Ma, J. M.; Liu, Z. F.; Lian, J. B.; Duan, X. C.; Kim, T.; Peng, P.; Liu, X. D.; Chen, Q.; Yao, G.; Zheng, W. J. Ionic liquids-assisted synthesis and electrochemical properties of Bi_2S_3 nanostructures. *CrystEngComm* **2011**, *13*, 3072–3079.

[6] Bao, H. F.; Li, C. M.; Cui, X. Q.; Gan, Y.; Song, Q. L.; Guo, J. Synthesis of a highly ordered single-crystalline Bi_2S_3 nanowire array and its metal/semiconductor/metal back-to-back schottky diode. *Small* **2008**, *4*, 1125–1129.

[7] Yao, K.; Gong, W. W.; Hu, Y. F.; Liang, X. L.; Chen, Q.; Peng, L. M. Individual Bi_2S_3 nanowire-based room-temperature H_2 sensor. *J. Phys. Chem. C* **2008**, *112*, 8721–8724.

[8] Harman, T. C.; Taylor, P. J.; Walsh, M. P.; LaForge, B. E. Quantum dot superlattice thermoelectric materials and devices. *Science* **2002**, *297*, 2229–2232.

[9] Boudjouk, P.; Remington, M. P., Jr.; Grier, D. G.; Jarabek, B. R.; McCarthy, G. J. Tris(benzylthiolato)bismuth. Efficient precursor to phase-pure polycrystalline Bi_2S_3. *Inorg. Chem.* **1998**, *37*, 3538–3541.

[10] Mizoguchi, H.; Hosono, H.; Ueda, N.; Kawazoe, H. Preparation and electrical properties of Bi_2S_3 whiskers. *J. Appl. Phys.* **1995**, *78*, 1376–1378.

[11] Liufu, S. C.; Chen, L. D.; Yao, Q.; Wang, C. F. Assembly of one-dimensional nanorods into Bi_2S_3 films with enhanced thermoelectric transport properties. *Appl. Phys. Lett.* **2007**, *90*, 112106.

[12] Ge, Z. H.; Zhang, B. P.; Shang, P. P.; Yu, Y. Q.; Chen, C.; Li, J. F. Enhancing thermoelectric properties of polycrystalline Bi_2S_3 by optimizing a ball-milling process. *J. Electron. Mater.* **2011**, *40*, 1087–1094.

[13] Zhang, L. J.; Zhang, B. P.; Ge, Z. H.; Han, C. G. Fabrication and properties of $Bi_2S_{3-x}Se_x$ thermoelectric polycrystals.

Solid State Comm. **2013**, *162*, 48–52.

[14] Chen, B. X.; Uher, C.; Iordanidis, L.; Kanatzidis, M. G. Transport properties of Bi_2S_3 and the ternary bismuth sulfides $KBi_{6.33}S_{10}$ and $K_2Bi_8S_{13}$. *Chem. Mater.* **1997**, *9*, 1655–1658.

[15] Grigas, J.; Talik, E.; Lazauskas, V. X-ray photoelectron spectra and electronic structure of Bi_2S_3 crystals. *Phys. Status Solidi B* **2002**, *232*, 220–230.

[16] Bhatt, R.; Bhattacharya, S.; Basu, R.; Ahmad, S.; Chauhan, A. K.; Okram, G. S.; Bhatt, P.; Roy, M.; Navaneethan, M.; Hayakawa, Y. et al. Enhanced thermoelectric properties of selenium-deficient layered $TiSe_{2–x}$: A charge-density-wave material. *Appl. Mater. Interfaces* **2014**, *6*, 18619–18625.

[17] Kyratsi, T.; Chung, D. Y.; Kanatzidis, M. G. Bi/Sb distribution and its consequences in solid solution members of the thermoelectric materials $K_2Bi_{8–x}Sb_xSe_{13}$. *J. Alloys Compd.* **2002**, *338*, 36–42.

[18] Cui, J. L.; Xiu, W. J.; Mao, L. D.; Ying, P. Z.; Jiang, L.; Qian, X. Thermoelectric properties of Ag-doped n-type $(Bi_2Te_3)_{0.9}$–$(Bi_{2–x}Ag_xSe_3)_{0.1}$ (x = 0–0.4) alloys prepared by spark plasma sintering. *J. Solid State Chem.* **2007**, *180*, 1158–1162.

[19] Yu, Y.-Q.; Zhang, B. P.; Ge, Z. H.; Shang, P. P.; Chen, Y. X. Thermoelectric properties of Ag-doped bismuth sulfide polycrystals prepared by mechanical alloying and spark plasma sintering. *Mater. Chem. Phys.* **2011**, *131*, 216–222.

[20] Ge, Z.-H.; Zhang, B.-P.; Liu, Y.; Li, J.-F. Nanostructured $Bi_{2–x}Cu_xS_3$ bulk materials with enhanced thermoelectric performance. *Phys. Chem. Chem. Phys.* **2012**, *14*, 4475–4481.

[21] Hicks, L. D.; Dresselhaus, M. S. Effect of quantum-well structures on the thermoelectric figure of merit. *Phys. Rev. B* **1993**, *47*, 12727–12731.

[22] Wang, D. B.; Shao, M. W.; Yu, D. B.; Li, G. P.; Qian, Y. T. Polyol-mediated preparation of Bi_2S_3 nanorods. *J. Cryst. Growth* **2002**, *243*, 331–335.

[23] Chen, J. S.; Qin, S. Y.; Song, G. X.; Xiang, T. Y.; Xin, F.; Yin, X. H. Shape-controlled solvothermal synthesis of Bi_2S_3 for photocatalytic reduction of CO_2 to methyl formate in methanol. *Dalton Trans.* **2013**, *42*, 15133–15138.

[24] Wang, D. S.; Hao, C. H.; Zheng, W.; Ma, X. L.; Chu, D. R.; Peng, Q.; Li, Y. D. Bi_2S_3 nanotubes: Facile synthesis and growth mechanism. *Nano Res.* **2009**, *2*, 130–134.

[25] Zhao, Y.; Xie, Y.; Jie, J. S.; Wu, C. Y.; Yan, S. Tectonic arrangement of Bi_2S_3 nanocrystals into 2D networks. *J. Mater. Chem.* **2009**, *19*, 3378–3383.

[26] Wang, Y.; Chen, J.; Chen, L.; Chen, Y. B.; Wu, L. M. Shape-controlled solventless syntheses of nano Bi disks and spheres. *Cryst. Growth Des.* **2010**, *10*, 1578–1584.

[27] Zhou, H. Y.; Xiong, S. L.; Wei, L. Z.; Xi, B. J.; Zhu, Y. C.; Qian, Y. T. Acetylacetone-directed controllable synthesis of Bi_2S_3 nanostructures with tunable morphology. *Cryst. Growth Des.* **2009**, *9*, 3862–3867.

[28] Okram, G. S.; Soni, A.; Prasad, R. The pH-controlled particle size tuning of nanocrystalline Ni in polyol synthesis method without additional cappant. *Adv. Sci. Lett.* **2011**, *4*, 132–135.

[29] Feldmann, C.; Metzmacher, C. Polyol mediated synthesis of nanoscale MS particles (M = Zn, Cd, Hg). *J. Mater. Chem.* **2001**, *11*, 2603–2606.

[30] Peng, Z. P.; Liu, M. Z.; Yu, C.; Chai, Z. L.; Zhang, H. J.; Wang, C. Preparation of nanoscale PbSe particles with different morphologies in diethylene glycol. *Nanoscale* **2010**, *2*, 697–699.

[31] Soni, A.; Okram, G. S. Resistivity and thermopower measurement setups in the temperature range of 5–325 K. *Rev. Sci. Instrum.* **2008**, *79*, 125103.

[32] Wubet, W.; Kuo, D.-H.; Abdullah, H. Effect of sintering temperature and duration on the structural and electrical properties of $CuBiS_2$ bulks. *J. Solid State Chem.* **2015**, *230*, 237–242.

[33] Razmara, M. F.; Henderson, C. M. B.; Pattrick, R. A. D.; Bell, A. M. T.; Charnock, J. M. The crystal chemistry of the solid solution series between chalcostibite ($CuSbS_2$) and emplectite ($CuBiS_2$). *Miner. Mag.* **1997**, *61*, 79–88.

[34] Tarachand; Sharma, V.; Ganesan, V.; Okram, G. S. Thermoelectric properties of CuS/Ag_2S nanocomposites synthesed by modified polyol method. *AIP Conf. Proc.* **2016**, *1731*, 110024.

[35] Lundegaard, L. F.; Makovicky, E.; Boffa-Ballaran, T.; Balic-Zunic, T. Crystal structure and cation lone electron pair activity of Bi_2S_3 between 0 and 10 GPa. *Phys. Chem. Miner.* **2005**, *32*, 578–584.

[36] Kyono, A.; Kimata, M. Structural variations induced by difference of the inert pair effect in the stibnite-bismuthinite solid solution series $(Sb, Bi)_2S_3$. *Amer. Miner.* **2004**, *89*, 932–940.

[37] Morgan, W. E.; Stec, W. J.; van Wazer, J. R. Inner-orbital binding-energy shifts of antimony and bismuth compounds. *Inorg. Chem.* **1993**, *12*, 953–955.

[38] Tang, A. W.; Qu, S. C.; Li, K.; Hou, Y. B.; Teng, F.; Cao, J.; Wang, Y. S.; Wang, Z. G. One-pot synthesis and self-assembly of colloidal copper(I) sulfide nanocrystals. *Nanotechnology* **2010**, *21*, 285602.

[39] Sam, M.; Bayati, M. R.; Mojtahedi, M.; Janghorban, K. Growth of Cu_2S/CdS nano-layered photovoltaic junctions for solar cell applications. *Appl. Surf. Sci.* **2010**, *257*, 1449–1453.

[40] Ghijsen, J.; Tjeng, L. H.; van Elp, J.; Eskes, H.; Westerink, J.; Sawatzky, G. A.; Czyzyk, M. T. Electronic structure of Cu_2O and CuO. *Phys. Rev. B* **1988**, *38*, 11322–11330.

[41] Zhao, Y. Y.; Chua, K. T. E.; Gan, C. K.; Zhang, J.; Peng, B.;

Peng, Z. P.; Xiong, Q. H. Phonons in Bi_2S_3 nanostructures: Raman scattering and first-principles studies. *Phys. Rev. B* **2011**, *84*, 205330.

[42] Koh, Y. W.; Lai, C. S.; Du, A. Y.; Tiekink, E. R. T.; Loh, K. P. Growth of bismuth sulfide nanowire using bismuth trisxanthate single source precursors. *Chem. Mater.* **2003**, *15*, 4544–4554.

[43] In, J.; Yoon, I.; Seo, K.; Park, J.; Choo, J.; Lee, Y.; Kim, B. Polymorph-tuned synthesis of α- and β-Bi_2O_3 nanowires and determination of their growth direction from polarized Raman single nanowire microscopy. *Chem.—Eur. J.* **2011**, *17*, 1304−1309.

[44] Denisov, V. N.; Ivlev, A. N.; Lipin, A. S.; Mavrin, B. N.; Orlov, V. G. Raman spectra and lattice dynamics of single-crystal α Bi_2O_3. *J. Phys.: Condens. Matter* **1997**, *9*, 4967−4978.

[45] Rolo, A. G.; Vasilevskiy, M. I.; Hamma, M.; Trallero-Giner, C. Anomalous first-order Raman scattering in III-V quantum dots: Optical deformation potential interaction. *Phys. Rev. B* **2008**, *78*, 081304(R).

[46] Trallero-Giner, C.; Debernardi, A.; Cardona, M.; Menéndez-Proupín, E.; Ekimov, A. I. Optical vibrons in CdSe dots and dispersion relation of the bulk material. *Phys. Rev. B* **1998**, *57*, 4664−4669.

[47] Ioffe, A. F. *Semiconductor Thermoelements and Thermo-electric Cooling*; Infosearch: London, 1957.